OPEN ACCESS

University of BRISTOL

Peer reviewed version

License (if available):
CC BY-NC

Link to published version (if available):
10.1002/esp.3948

Link to publication record in Explore Bristol Research
PDF-document

University of Bristol - Explore Bristol Research

General rights

Architecture of the deep critical zone in the Río Icacos watershed (Luquillo Critical Zone Observatory, Puerto Rico) inferred from drilling and ground penetrating radar (GPR)

Joe Orlando[1], Xavier Comas[2], Scott A. Hynek[1,4], Heather L. Buss[3], and Sue L. Brantley[1,4]

[1]: Department of Geosciences, Pennsylvania State University, State College, PA

[2]: Department of Geosciences, Florida Atlantic University, Davie, FL

[3]: School of Earth Sciences, University of Bristol, Bristol, UK

[4]: Earth and Environmental Systems Institute, Pennsylvania State University, Univ. Pk PA

Abstract

In the critical zone, surficial bedrock interactions result in the formation of a mantle of chemically- and physically-altered material defined here as regolith. In the watershed of the Río Icacos, an upland river draining the Luquillo Mountains in tropical Puerto Rico, we explored the influence of lithology (quartz diorite versus hornfels-facies volcaniclastic rock) on weathering. Regolith profiles were studied by drilling boreholes and imaging the subsurface using ground penetrating radar (GPR). Overall, the regolith structure is not laterally continuous but rather is punctuated by zones of deep fractures that host in situ weathering, corestones, and colluvial material. GPR images of these vertical zones show reflectors at 15–20 m depth. Thus, the architecture of the critical zone in the upper Luquillo Mountains is highly dependent on lithology and its influence on fracture development. At the highest elevations where hornfels overlies quartz diorite, positive feedbacks occur when the water table drops so that oxidative weathering of biotite in the more felsic rock creates microfractures and allows deeper infiltration of meteoric waters. Such exposure results in

some of the fastest weathering rocks in the world and may contribute to formation of the knickpoint in the Río Icacos watershed. This work represents the first study combining GPR and drilling to look at the structure of the deep critical zone and demonstrates: 1) the importance of combining direct methods (such as drilling) with indirect methods (such as GPR) to understand the architecture of the critical zone in tropical systems; and 2) the interplay of the surficial stress regime, lithology and climate in dictating the architecture of weathering.

1. Introduction

The surface of the Earth is covered by a mantle of chemically and physically altered material referred to here as regolith that overlies the unaltered bedrock. The depth interval where unaltered bedrock transforms to regolith is located at depths varying typically between 0 to 1000s of meters (Ollier, 1984; White and Blum, 1995; Brantley et al., 2013). The deepest extents of weathering on Earth are found in the wet tropics where temperatures and water fluxes are high enough to promote fast weathering and where water tables may reach depths of hundreds of meters (Ruxton et al., 1959; Ollier, 1984; Nahon, 1991; Brantley et al., 2013). For example, White and Blum (1995) compared several watersheds on granitic lithologies in different climatic regimes and discovered that the weathering fluxes of Si and Na increase linearly with precipitation and exponentially with temperature. White et al. (1998) argued that the fastest weathering granitic material was observed in Puerto Rico in what is now known as the Luquillo Critical Zone Observatory (LCZO). While others have since documented other tropical sites with faster weathering, the LCZO serves as an epicenter for intense investigations of the fast-weathering denudation endmember.

One defining feature of the LCZO that influences the position of the bedrock-regolith interface is a major knickpoint that occurs in the lower reaches of Río Icacos watershed

where several other tributaries join the mainstream to form the Río Blanco. Across this knickzone, elevation changes from ~600 to ~300 masl over a lateral distance of ~1500 meters (~15% slope). A knickpoint is a sharp change in the slope of a fluvial channel often attributed to differential erosion due to changes in lithology (Harris, 1968). Although no general change in lithology has been noted across the elevation of the knickpoint in the channel where the Río Icacos mostly incises quartz diorite, a narrow zone of hornfels crosses the stream channel approximately coincident with the knickpoint location (Figure 1). Above the knickpoint, the gradient in the longitudinal profile of the Rio Icacos is very low (0.9%) over a lateral extent of about ~2300 meters (Brocard et al., 2015). In this near-flat reach, quartz-rich sand layers are punctuated by a few protruding corestones and, in some places where the quartz is largely removed, in situ formation of corestones with fractured rindlets are observed in the bedrock channel.

This knickpoint has been attributed by Brocard and colleagues to ongoing incision into a landscape that was graded to the sea level of the ancient El Yunque Island before the island was uplifted and tilted, ~3.3 Ma (Brocard et al., 2015). In that model, ongoing denudation is acting to propagate the knickpoint headward. Observations along the longitudinal profile of the Río Blanco have revealed that above the knickpoint, the quartz diorite spheroidally weathers to form corestones surrounded by fractures that subtend centimeter-thick rindlets of partially weathered rock (Turner et al., 2003; Fletcher et al., 2006; Buss et al., 2008; Brantley et al., 2011; Orlando, 2014). Thus, above the knickpoint where the river incises bedrock, ubiquitous corestones and rindlets are observed in the channel whereas below the knickpoint, extensive *in situ* corestone formation has not been observed. Where spheroidally weathered corestones have been observed in the river bed below the knickpoint, they have generally been attributed to downhill transport from higher elevations (Fletcher and Brantley, 2010).

Systematic studies of the regional architecture of the bedrock-regolith interface in the LCZO are generally lacking due to the difficulties of access within the steep terrain. Better understanding of the architecture of the bedrock-regolith interface is critical since it often can control water transmission and storage, input of mineral and solute flux to the biosphere and hydrosphere (Ruxton et al., 1959; Ollier, 1988; Buss et al., 2008; Drake et al., 2009; Brantley et al., 2011). Previous efforts to understand the geometry of the bedrock-regolith interface in the LCZO have included studies based on field observations and modeling (Fletcher and Brantley, 2010; Brantley et al., 2011), chemical, petrographic and spectroscopic analysis (Buss et al., 2008), or isotopic techniques (Dosseto et al., 2012). Only a few geophysical studies have been completed. For example, Schellekens et al. (2004) completed electrical soundings in combination with hydrometric and soil geochemistry datasets to understand stormflow generation processes in a watershed on the Luquillo mountain flanks developed on volcaniclastic rocks. Another previous study by Larsen (1995) used seismic refraction to investigate two landslides in the Caribbean National Forest in Puerto Rico. Previous studies have developed conceptual models depicting the transition from bedrock to corestones and regolith on the quartz diorite such as that shown in Figure 1a (Brantley et al., 2011). Direct sampling from deeper parts of the critical zone using drilled boreholes has also been recently conducted reaching depths down to 37 m (Buss et al., 2013). Despite these efforts, the overall geometry of the bedrock-regolith interface in the LCZO is still uncertain, understandably related to the limitations of these methods to provide a spatially continuous record of measurements. For example, boreholes represent point measurements of the subsurface at one specific location that are not necessarily representative of that subsurface at other locations, even if just a few meters away.

In contrast, near-surface geophysical techniques can provide information of the subsurface beyond point measurements at a spatial resolution ranging from m to cm

depending on the technique. Near-surface geophysical techniques have been used for more than three decades to explore the bedrock-regolith interface in a variety of environments. For example, Hunter et al. (1984) and Dasios et al. (1999) both used shallow seismic methods to map the topography of the overburden-bedrock interface. Researchers have also used ground penetrating radar (GPR) to map the regolith-bedrock interface (Zhang et al., 2014). Shafique et al. (2011) used electrical resistivity to image the regolith-bedrock interface and estimate regolith thickness in northern Pakistan, while Chaudhuri et al. (2013) and Braun et al. (2009) used a similar approach in watersheds in India. Holbrook et al. (2014) used a combination of seismic and electrical resistivity to estimate variability of regolith thickness in several environments across the Southern Sierra Critical Zone Observatory. Although the geophysical techniques used (and thus the physical property inferred from the measurement) may be different for each particular study, geophysical surveys result in an indirect measurement of the bedrock-regolith interface as represented by a contrast in a certain physical property. For that reason it is critical that indirect measurements are constrained with direct observations.

GPR is a highly effective technique that can reveal structural information about the subsurface. GPR data are highly dependent upon: a) the presence of homogeneous materials with no internal changes in physical attributes, and thus no contrasts in dielectric permittivity; b) electromagnetic (EM) wave attenuation due to the presence of electrically conductive material, such as wet clay materials with high values of ionic conductivity and cation exchange capacity (CEC); or c) the natural attenuation of the EM wave with depth, which depends on the depth of penetration associated with antenna frequency and the nature of the subsurface material. Here, a GPR study was designed to test these factors to allow better understanding of the architecture of weathering in the Río Icacos watershed.

We used a combination of direct and indirect measurements to characterize the bedrock-regolith interface at several locations in the LCZO. To our knowledge, this is the first study that combines drilling results with ground penetrating radar (GPR) surveys to image the structure of the deep critical zone. An array of ground penetrating radar (GPR) measurements were collected at five different locations within the Río Icacos watershed, three of them coinciding with the location of previously drilled boreholes. GPR measurements using an array of 50, 100, and 200 MHz unshielded antennas and a 160 MHz shielded antenna were performed and included a set of common offsets to generate two-dimensional (2D) profiles with depth and common midpoint surveys to generate one-dimensional (1D) models of electromagnetic (EM) wave velocity.

2. Study site and geological setting

The Luquillo Critical Zone Observatory (LCZO) is part of a network of ten observatories in the USA that make up the National Science Foundation Critical Zone Observatory (CZO) Program. These observatories focus on the interaction of components of the critical zone, defined as the layer extending from the top of the vegetation to the base of the weathered bedrock. The LCZO is located in the Luquillo Mountains of northeastern Puerto Rico, an area that has historically been a locus of research activity for researchers within the US Forest Service (USFS), the US Geological Survey (USGS) as well as university researchers. Several observatory programs, including the USFS Luquillo Experimental Forest (LEF), the USGS Water Energy and Biogeochemical Budgets (WEBB) program, and an NSF Long Term Ecological Research site (LTER) have operated in the mountains over the last few decades. Within the context of the CZO network, the LCZO represents the highest mean annual temperatures (19–25 ˚C) and rainfall (3000 to >5000 mm

y^{-1}), the greatest net primary productivity (> 10 Mg/ha y^{-1}), and the most abundant

biodiversity (Brown et al., 1983; Scatena, 1989).

Located within the Luquillo Mountains, El Yunque National Forest is the only

tropical rain forest in the United States National Forest system. From the northern coast of

Puerto Rico at Punta Miquillo to the highest point of the Luquillo Mountains (El Toro) there

is a change in relief of 1,075 meters over a lateral distance of approximately 17 km. The

Luquillo Mountains are composed of uplifted andesitic to basaltic volcaniclastic sedimentary

rocks of the Fajardo Formation. This formation grades to rocks of similar composition within

the younger Tabonuco (~113–110 Ma) and the Hato Puerco (~100–84 Ma) Formation

(Seiders, 1971). These rocks were intruded in the Tertiary by the Río Blanco (~46.2–45.7

Ma) quartz diorite pluton (Cox et al., 1977). Contiguous to the quartz diorite, the

volcaniclastics have been metamorphosed to form a hornfels-facies aureole which forms the

highest ridges of the LEF (Figures 1b and 1c).

The island of Puerto Rico is on the Caribbean Plate and has experienced many stages

of uplift and erosion (ten Brink et al., 2009). The last stage is thought to have involved a

rapid tilting event occurring over 14–40 ky that took place 3.3 Ma (ten Brink, 2005), causing

the southern edges of the island of Puerto Rico to lift upwards as much as 1,300 m. Incision

into the contact metamorphic system occurred mostly due to two major rivers, the Río

Blanco, and the Río Mameyes which trend south-southeast, and northeast respectively

(Figures 1b and 1c). The Río Icacos watershed (i.e., the headwaters of the Río Blanco) is

basically a bowl incised into the underlying quartz diorite with ridgelines of hornfels facies

metavolcaniclastic rocks outcropping in the north and east-southeast. One narrow zone of

hornfels extends along the downstream margin of this perched watershed, roughly coincident

with the point where the river spills over the knickpoint (Figure 1). In contrast, the north-

flowing Río Mameyes has incised predominantly into the volcaniclastic rocks, only exposing

the hornfels ridges at the uppermost elevations with small exposures of the quartz diorite only in one sub-catchment.

A total of five sites were investigated in this study using a combination of GPR, drilling, hand augering, and outcrop observation. Three of the sites were located on quartz diorite (LGW1, LGW2, and PB, as shown in Figures 1b and 1c), while the remaining sites were located on the hornfels along the ridgeline between the Icacos and Mameyes rivers (EP1 and CD2). While GPR surveys were performed in all sites, results from drilling were only available at LGW1, LGW2, and EP1. GPR results at sites PB and CD2 were constrained with hand augering and some limited exposures (i.e. outcrops). Surveys were designed to complement direct observations of regolith (drilling, hand augering, outcrops).

3. Methods

3.1. Augering and Outcrop Sampling

At CD2 (on hornfels), regolith was hand augered with a solid flight auger attached to a 7.6 cm (O.D.) bucket suited for retrieval of clay rich material. At site PB (on quartz diorite), a ~30 meter long, ~3 meter tall exposed road cut is exposed, revealing a set of corestones ranging in size from 0.5 to 2 m within a saprolite matrix. Each set consists of multiple centimeter-thick rindlets that that grade upward to saprolite (Turner et al., 2003; Buss et al., 2008). At site EP, hornfels-derived outcrops (up to 8 to 10 m tall) were observed in several nearby road cuts.

3.2. Drilling

Drilling was conducted in three locations: a) one hole was drilled at LGW1 by Geo Cim Inc. (Guaynabo, Puerto Rico) in June 2010, using a hydraulic rotary drill with diamond impregnated drill bits (9.6 cm diameter HQ) with untreated water pumped from nearby streams as drilling fluid; b) three holes were drilled at LGW2 (A, B, and C) by Suelos Inc.

(San Juan, Puerto Rico) between June and September, 2012, using a CME 750 hydraulic

rotary drill rig equipped with an H W/L 3 (9.6 cm diameter) wireline core barrel, and using

tap water transported from San Juan, PRASA (Puerto Rico Aqueduct and Sewer Authority);

and c) one hole at EP1 by Suelos Inc. in March, 2013, following the same approach as for

LGW2 but using water extracted from a private well in Arecibo, Puerto Rico. Drilling at

LGW2 and EP1 were initiated with hollow flight augers and split spoon sampling through the

overburden in ~1 m increments. DOSECC (Drilling, Observation and Sampling of the Earths

Continental Crust) provided on site technical advising and core catcher baskets to capture

softer material that would have fallen out of the drill core tube with a standard core catcher.

Recovery of drilled material in all boreholes was logged. Solid cores and consolidated

weathered material were recovered where possible and fractures within solid rocks were

noted as a function of depth.

3.3. Ground Penetrating Radar (GPR)

GPR uses a transmitting antenna (Tx) to generate a high-frequency electromagnetic

(EM) wave (typically between 10-2,000 MHz) that penetrates the subsurface and is returned

to a receiving antenna (Rx) as a sequence of reflections from certain interfaces (Annan,

2009). Reflecting interfaces are characterized by contrasts in physical properties such as

stratigraphic or structural boundaries, changes in bulk density or porosity, or changes in water

saturation. The velocity of this electromagnetic (EM) wave is primarily controlled by the

relative dielectric permittivity (ε_r) of the subsurface media, a property strongly dependent on

the geological material properties, that ranges between 1 (for air) and 81 (freshwater at 20˚C).

While natural attenuation of the signal with depth induces loss of energy as the wave travels

deeper, attenuation is frequency-dependent and is affected by other factors such as

conduction losses related to changes in electrical conductivity. For that reason, EM waves do

not propagate efficiently through materials such as seawater or clays such as smectite and

vermiculite with high cation exchange capacity, CEC (due to high electrical conductivity) (Walker et al., 1973). High conductivity materials dissipate most of the EM energy as heat, resulting in attenuation of the EM signal and a dramatic reduction in the depth of penetration (Cassidy, 2009). For that reason GPR is most useful when operating in low electrical loss materials (Annan, 2009). Previous studies of the Icacos and Bisley watersheds have identified kaolinite, a low CEC clay, as the dominant mineral in the regolith (White et al., 1998). Since penetration depth of GPR is inversely related to clay content, it is expected that penetration depths would be enhanced in low CEC clay fractions dominated by kaolinite, gibbsite and goethite, as compared to clay fractions dominated by smectite or vermiculite (Daniels, 2004). To accommodate truck-based drill rigs, all drilling sites were on roads. At these localities, GPR was used to survey along the side of the road (route 191 in Figure 1c) or directly over the road bed. Multiple observations from all sites indicate that the road fill is <1 m thick. At the PB outcrop, GPR surveys were collected by walking over the top of the roadcut. At the site of hand augered borehole CD2, surveys were conducted in the forest approximately 15 m from the road.

GPR surveys were performed in two different modes: a) common offset (CO) profiling where the Tx and Rx antennae are moved synchronously along the ground maintaining a fixed distance (Figure 2a); and b) common midpoint (CMP) profiling, based on a Tx and Rx antenna progressively separated from a center midpoint (Figure 2b). In the first case, the resulting CO profile typically shows a series of reflections commonly interpreted as hydrogeological interfaces (such as sedimentary interfaces or layers with contrasting water contents) that resemble a geologic cross-section where the vertical scale is expressed as a two-way travel time and is later converted into a depth (Figure 2a). To complete the conversion, the velocity of the EM wave has to be estimated. In some sites (such as PB), the presence of isolated point reflectors (Neal, 2004) resulted in the presence of diffraction

hyperbolas in CO profiles, allowing the construction of 2D models of velocity. In the second case, the CMP approach results in a radar reflection profile that depicts how travel time increases as a function of antenna separation (i.e. distance). EM wave travel time increases linearly for both the portion of the EM wave that travels through the air (air wave) and through the air-ground interface (ground wave). The travel time becomes hyperbolic for reflection events below the subsurface (Figure 2b). The relationship between travel time-antenna separation (i.e. time-distance) is then used to develop one-dimensional (1D) models of EM wave velocity along the center point (i.e. midpoint) of the survey. Uncertainty in velocity estimates from 1D models as based on repeatability of measurements averaged 0.005 m ns^{-1} or about 5 %.

GPR surveys were measured using a Mala RAMAC GPR with 50, 100 and 200 MHz unshielded antennae and a 160 MHz shielded antenna to identify the best experimental setup to maximize both vertical resolution and depth of penetration at each site. It is important to note that as frequency increases resolution also increases while depth of penetration decreases. Trace spacing ranged from 0.1–0.2 m, with sixteen stacks per trace, and a sampling time window ranging between 500–1000 ns depending on antennae frequency. A combination of manual keyboard and hip-chain was used to trigger data acquisition. Profiles shorter than 50 m were triggered manually with 0.1 m trace spacing, while a hip-chain was used for profiles longer than 50 m with 0.2 m trace spacing. GPR data processing was performed using ReflexW by Sandmeier Scientific. Steps were limited to: a) a "dewow" filter over a 10ns time-window; b), application of a time-varying gain; c) a bandpass filter; d) a static correction; and in some cases, e) Kirchhoff migration based on a single EM wave velocity as determined from the CMP profiles.

The nature of the signal propagation through the subsurface dictates both vertical and horizontal resolution (Neal, 2004; Annan, 2009). For practical purposes, vertical resolution is

proportional to velocity and mainly corresponds to one-quarter of the dominant wavelength, while horizontal resolution is dictated by the width of the Fresnel zone. For example, vertical resolution when considering average velocities of 0.1 m ns^{-1} range between 0.25 m and 0.12 m when using 100 MHz and 200 MHz antennas respectively. Single rindlets on corestones, which measure ~0.02 m, are likely not visible at this resolution, but a stack of rindlets (>0.25 m) should be resolvable. In terms of horizontal resolution, the Fresnel zone has an approximate volume of 0.6 m^3 (or a radius of 0.8 m in footprint) for a 200 MHz antenna reflecting from an interface at 2 m depth. This spatial resolution affects the ability to image corestone boundaries at depth.

4. Results

4.1. General drilling observations

The lowest-elevation borehole, LGW1, was drilled just above the knickzone at 648 masl (meters above sea level). At a somewhat lower elevation than LGW1, a roadcut (PB, 628 masl) was also thoroughly investigated in an area still relatively near the knickzone. The highest-elevation borehole, EP1, was drilled at 780 masl high above the knickzone on the opposite side of Rio Icacos near the top of the watershed. LGW2 (740 masl) was drilled almost as high as EP1 but on the same side of the catchment as LGW1, also high above the knickzone. Hornfels outcrops define the uppermost ridges on both sides of the catchment (i.e. the EP1 and LGW2 sides), but LGW2 was drilled where local outcrops are quartz diorite: the hornfels outcrops near LGW2 but at a slightly higher elevation.

The LGW1, LGW2, and EP1 boreholes ranged in depth between 25 to 40 m (Figure 3, Table 1). The bottommost rock was assumed to be intact and unaltered bedrock at each borehole location. One borehole at LGW2 (LGW2A, where drilling ceased for technical reasons) did not reach intact bedrock. The bedrock at the base of all three of the boreholes is

quartz diorite, regardless of the rock type at the surface. The cores of quartz diorite recovered from the base of all boreholes were predominantly coarse grained, homogeneous, grey, and dominated by phenocrysts of quartz, plagioclase, biotite and hornblende. Occasional xenoliths ranging in size from ~2–25 cm were identified by their fine-grained nature and darker color. Sometimes, when fractures were encountered during drilling, the weathered material within the fracture was recovered. However, other fractures yielded no recoverable material.

At each site, three types of material were observed or recovered: i) road fill, ii) disaggregated coarse-grained particulate material (sometimes intact as core and sometimes as a slurry of weathered material mixed with drilling fluids), and iii) intact rock either with or without fractures. No further consideration is given here to the road fill material. The type (ii) material looks texturally very much like saprolite observed in outcrop or in hand-augered cores and is therefore referred to here as saprolite. However, we note that this definition is only based on the texture, because drilling mostly did not allow observation of the other notable characteristic of saprolite, namely that the disaggregated material has formed by isovolumetric weathering of bedrock in place, retaining evidence of the original rock structure. Figure 3 shows the distribution of this "saprolite" with depth in the context of the water table elevations (blue shaded zone) measured by hand between 08/26/2010 and 03/02/2014 after accounting for topography at each drilled site.

In the highest borehole (EP1), no hornfels bedrock was intersected even though i) the location was on a hornfels ridge, ii) hornfels outcrops were observed nearby, and iii) a small hornfels pebble was recovered in the borehole from the upper 7 meters of drilling. However, drilling returned a 6–7 m sequence of saprolite that had a composition consistent with a hornfels parent. Beneath this, the borehole passed through a sequence alternating between quartz diorite-derived saprolite and intact quartz diorite and quartz diorite-derived saprolite.

In contrast, the lowest borehole, LGW1 (located 130 m below EP1 and very near the knickzone), is mainly characterized by road fill + saprolite above a highly fractured quartz diorite depth interval located at ~5 m depth. This set of fracture-subtended rock discs was identified as a 50-centimeter thick set of about 25 rindlets and was underlain by one relatively shallow fracture and a 20 m depth interval of unfractured quartz diorite (Figure 3). Fracturing is further discussed in the next section. At higher elevation on the quartz diorite at roughly the elevation of EP1, LGW2 (boreholes A, B, and C) are characterized by alternating sequences of quartz diorite and quartz diorite-derived "saprolite". A very minor lens of hornfels rock was recovered from ~10 m depth in LGW2C, consistent with the location of the site near the top of the watershed where hornfels-facies rock defines the ridge and the contact metamorphic aureole. At least one large void was encountered at LGW2B between 8 and 9 meters below land surface (shown on Figure 3 as a grey zone without stipple pattern), which resulted in a 1.5 m sudden drop of the drill bit during drilling. Coincidentally, a piece of cement that was used to grout the casing for the LGW2A borehole was recovered from just below the fourth corestone in the LGW2B borehole (2 meters away from LGW2A) from a depth of ~11 meters.

4.2 Fracture observations during drilling

In recovered rock core, veins (dashed lines) and fractures that were obviously present pre-drilling (black lines) were observed and noted (Figure 3). Pre-existing fractures were identified as breaks that showed evidence of weathering. When sub-parallel fractures were observed in sub-pieces of intact core with a spacing on the order of centimeters, or when centimeter-sized discs of core were recovered that were subtended by weathered surfaces, they were assumed to be rindlets, i.e., centimeter-thick pieces of weathered or unweathered rock subtended by spheroidal fractures (Buss et al., 2008). The presence of rindlets was used

as one criterion for identifying corestones. Rindlets were identified at 5 m depth in borehole LGW1, at 14-20 m depth in LGW2, and at 39 m depth in EP1. In each of the boreholes, the deepest fracture showing oxidation features (red staining or biotite yellowing, shown on Figure 3 as a red line) was identified and interpreted as the deepest extent of interaction with a significant flux of oxygen-rich water. The most concentrated number of rindlets was always observed to lie directly above the bedrock in each borehole (i.e. Figure 3).

The thinnest total regolith (5 meters), the most highly fractured rock (quartz diorite with 25 fractures within 50 cm) and the largest depth interval of competent rock (20 meters) was observed at the lowest elevation borehole LGW1, drilled at an elevation just above the knickpoint (Table 1). All of the fractures except one in the LGW1 borehole were concentrated in the single rindlet set observed at the bedrock-regolith interface (Buss et al., 2013). In contrast, the thickest regolith (14 meters) and the lowest number of fractures (9) was encountered in the highest elevation borehole, EP1, which is also located at a hornfels ridgeline and highest in elevation above the knickpoint.

4.3. GPR surveys

GPR measurements at each study site include: a) common midpoint (CMP) surveys used to develop one-dimensional (1D) models of EM wave velocity with depth at selected locations, and b) common offset (CO) surveys used to develop cross sections based on 2D distributions of reflections with depth and coinciding with the location of wells and/or exposures. Although profiles were collected over Route 191, any effects of the road fill are contained within the ground coupling zone (Figure 2) and are therefore irrelevant. A 20 m CO profile intersects well LGW1 at 7 m along the profile (Figure 4a) and reveals a sequence of isolated reflectors that almost completely disappear below ~120 ns. This depth coincides with the regolith-bedrock interface at about 5–6 m detected in the borehole. The presence of

fractures at that interface coincides with a set of 4–5 reflectors in the CO record. The one dimensional model of velocity from the CMP profile (Figure 4b) is consistent with CO and drilling results and shows a signal velocity progressively increasing with depth from 0.1 m ns^{-1} at the surface to 0.15 m ns^{-1} at about 6 m deep. Figure 4c shows a 230 m long extension southward along Route 191 (Figure 1c) from the CO profile in Figure 4a. This extension followed the road which contours the land surface and remains relatively flat along the traverse. Where the road crossed small tributary valleys (i.e. Route 191 in Figure 1c bending westwards following topographic contours), deep chaotic reflectors are imaged to nearly 20 m depth. This depth is much greater than the depth of road fill material (~1m) and also much greater than the maximum depth of the valleys observed at the surface (4–5 m). Figure 4c depicts the presence of sharp vertical boundaries (centered at distances of ~70m, ~125m, and ~155m from the start of the transect) characterized by sequences of chaotic reflectors reaching 15 to 20 m deep and extending 10 to 35 m along the transect. In every case, these areas of chaotic reflectors observed in GPR were observed to align with locations where the road crosses the observed valleys. These areas of chaotic reflections contrast with the overall lack of reflectors surrounding well LGW1 and the lack of reflections for interfluves between the small tributary valleys.

Figure 5 shows two sets of GPR CO profiles and 1D models near well LGW2. Figure 5a represents an extension of Figure 5b which crosses well LGW2B and LGW2A at about 63 and 65 m along the profile, respectively. Figure 5b shows a sequence of continuous sub-parallel reflections distributed between 0 and 10–12 m depth that coincide with an alternating sequence of quartz diorite and "saprolite" material as detected in wells LGW2A and B. Below a depth of 12 m, reflectors almost completely disappear coinciding with the presence of a thick (i.e. 6–7 m) sequence of weathered material. The purpose of the profile in Figure 5a (situated topographically as much as 4 m higher than the profile in Figure 5b) was to test

whether the attenuation detected at about 12 m in the GPR profile in Figure 5b was related to lithology (i.e. a thick saprolite) or to the natural attenuation of the GPR signal with depth. Since the reflections in Figure 5a are deeper than in Figure 5b, reaching depths that exceed 400 ns (or close to depths of 20 m), attenuation at this site is more likely to be related to physical characteristics of the regolith than to the natural attenuation of the EM wave with depth. This supports the existence of a laterally extensive zone at depth that may be heavily weathered and/or may coincide with the water table. The velocity models from CMPs at two different locations (i.e. CMP21 located 21 m along the profile and CMP12 located at 58 m along the profile as shown in Figure 5c and 5d, respectively) also are consistent in depicting alternating sequences of layers with 0.08 and 0.1 m ns^{-1} velocities associated with the presence of saprolite and corestones, respectively.

GPR results from site PB are shown in Figures 6 and 7 along with a sketch based on photographs of the 30 m long outcrop exposure along the Route 191 roadcut. The outcrop shows a 4 meter thick sequence of stacked corestones surrounded by rindlets within a matrix of saprolite. GPR profiles were collected on top of the outcrop to compare the radar response to the materials exposed in the outcrop. Figure 6a shows a schematic of the spatial relationships of corestones and rindlets within the exposure, which contains a total of 8 exposed corestones (c1-c8) and three sets of rindlets (r1-r3). As observed in the outcrop, the corestones are rounded blocks of homogenous quartz diorite, surrounded by 1-m thick sets of 10–40 rindlets (centimeter-thick fracture-subtended layers of quartz diorite). These have been well described in the literature and interpreted as evidence of the spheroidal weathering mechanism of corestone formation (Turner et al., 2003; Fletcher et al., 2006; Buss et al., 2008). The matrix surrounding corestones is observed in the outcrop to be saprolite that still contains evidence of rindlets or rock texture. Further description of this site can be found in Buss et al. (2008).

The unique presence of numerous diffraction hyperbolas on pre-migrated CO profiles allowed generation of a 2D model of velocity of the outcrop (Figure 6b) and showed velocity values ranging between 0.060–0.080 m ns^{-1}, i.e., very consistent with 1D models from CMPs. As shown in Figure 6b corestones are characterized by higher velocities (0.075–0.080 m ns^{-1}) when compared to rindlets (0.060–0.065 m ns^{-1}) and surrounding saprolite (0.065–0.070 m ns^{-1}). This is consistent with previous estimates showing higher velocities for quartz diorite when compared to regolith (i.e. site LGW1 in Figure 4, or site LGW2 in Figure 5). Migrated GPR CO profiles (Figure 6c) also show correspondence between lack of reflections and presence of corestones (i.e. c3 or c7 in Figure 6c) while rindlets are characterized by sequences of clearly curved reflections mostly aligned parallel to corestone boundaries (i.e. r3 and c7 in Figure 6c).

Figure 7 shows a 1D model of velocity for the PB outcrop, inferred from a CMP GPR survey collected at 6 m distance along the CO shown in Figure 6c. The model shows a gradual increase in velocity from 0.065 to 0.09 m ns^{-1} for the first 4–5 m, followed by a subsequent increase between 0.1 to 0.14 m ns^{-1} between 4–8 m depth. A consistent velocity of 0.14 m ns^{-1} is found below 8 m and coincides with the values obtained for bedrock in site LGW1 below the interface regolith-bedrock (Figure 4b).

GPR results for sites CD2 (the hand augered site located 83 m above EP1 on hornfels) and EP1 are shown in Figure 8. Only at CD2 were angular hornfels corestones observed commonly at the ground surface. Site EP1 was drilled below 40 m, but hand augering at site CD2 reached sampling depths down to 9 m before auger refusal. In both cases a thick layer of clay-rich regolith was present, recorded from drilling to a depth of 14 m at site EP1 (Figure 3) and from hand augering to a depth of 9 m at site CD2. Several outcrops along the road (i.e. Figure 8d) at elevations similar to or higher than EP1 and CD2 show clay-rich regolith deposits up to 14m thick overlying outcrops of hornfels rock. Common offsets at both CD2

(Figures 8a and 8b) and EP1 (Figure 8e) are characterized by a sequence of sub-parallel and wavy reflectors at depths between 0–5 m. Reflectors are absent below 5 m. To confirm that lack of reflections below 5 m was related to signal attenuation due to the nature of the geological materials rather than the natural attenuation of the EM wave with depth, two different antennae were used (50 MHz and 100 MHz antennas as shown in Figure 8a and 8b respectively). These showed a consistent attenuation below 5 m. 1D models of velocity from CMP profiles at both sites (CD2 in Figure 8c and EP1 in Figure 8f) also show consistent velocities between sites averaging 0.06–0.07 m ns^{-1}.

5. Discussion

5.1. General observations

The drilling observations were surprising in several ways: for example, i) drilling recovered no hornfels rock from EP1 despite the presence of nearby outcrops of hornfels, ii) when regolith was present on hornfels, it was very deep, and ii) a small amount of hornfels rock was recovered from LGW2 where quartz diorite was observed in outcrop. The presence of hornfels rock in LGW2 probably just documents minor entrainment of volcaniclastic sedimentary protolith in the quartz diorite pluton. Indeed, the pluton – aureole contact has been mapped to contain many angular, presumably fracture-controlled protrusions (Seiders, 1971). In addition, the hornfels in LGW2 could have derived from colluvial material from a landslide derived from the hornfels ridgeline above LGW2. Such a landslide is possible given the borehole's location near the upper end of a headwater channel. However, the observation of in situ rindlets observed at 14 and 20 m depth also attest to in situ corestone and saprolite formation in LGW2. We were also surprised that the regolith on hornfels at both EP1 and CD1 was as thick as observed, given that hornfels is the "ridge-forming unit" and hornfels

rock fragments (tens of centimeters in dimension) litter the upland land surface. While variability in thickness of regolith is expected, variations from 0 (outcrop) to 14 m at EP1 seemed especially large over short distances.

The hornfels composition is andesitic, i.e., more mafic than the quartz diorite. Based on observations worldwide, we would have predicted a thinner rather than thicker regolith on the more mafic EP1 rock than at LGW1 or LGW2 (if they were all eroding at similar rates). Specifically, Bazilevskaya et al. (2013) have shown that for two lithologies that have weathered long enough to attain a steady state regolith thickness at a ridgetop in a similar climate, the more mafic rock will generally be thinner than the more felsic rock as long as they are eroding at comparable rates.

In fact, the mafic hornfels is known to be eroding and weathering very slowly compared to the "bowl-forming unit", the quartz diorite. Such slow rates of denudation are common for massive mafic rocks which have been observed to limit infiltration of meteoric water (Bazilevskaya et al., 2013). Lack of infiltration is manifested on the hornfels by pooling of water which we have observed during precipitation events. For example, the only known bogs in the Luquillo Mountains occur on the hornfels-grade metamorphic rocks (Ogle, 1970). Infiltration into both the hornfels protolith and regolith are likely to be slow due to the lack of fractures and lack of abundant quartz (which can hold open porosity). Dissolution of the most abundant primary minerals, feldspar and pyroxene (Orlando, 2014), has also left a clay-rich regolith that limits infiltration. Orlando (2014) reported low quartz content and the presence of chloritic or illitic clays in the CD2 borehole and upper 7 m of EP1 material.

In contrast, although the quartz diorite protolith is massive like the hornfels, ample evidence has shown that weathering-induced fracturing occurs during oxidative weathering of the rock, enhancing infiltration of meteoric fluids (Fletcher et al., 2006; Buss et al., 2008). Specifically, when oxygen-containing waters penetrate the quartz diorite, biotite oxidation is

thought to create a positive feedback that produces more fractures and accelerates more chemical reactions through the mechanism of spheroidal weathering (Fletcher et al., 2006; Buss et al., 2008).

At EP1 and CD2, we nonetheless observed very thick regolith. We only have speculations as to why thick regolith forms on hornfels at those sites and not at the uppermost ridgetops. For example, one possibility is that the hornfels protolith under EP1 and CD2 was more fractured a priori than the protolith under the ridges, and therefore allowed more infiltration of the major weathering reagents (H_2O, O_2, CO_2, organic acids) into the rock. This would have resulted in faster weathering advance. Once O_2 infiltrated deep enough to reach the underlying quartz diorite, weathering of the overlying hornfels could have in turn accelerated as the deeper felsic rock oxidatively fractured and promoted even faster drainage of meteoric water. This idea is addressed again at the end of the paper.

5.2. Radar facies, EM wave velocities and drilling observations as related to subsurface characteristics

GPR surveys at the study sites depict contrasts in subsurface materials with respect to GPR reflection configuration and continuity. Such differences are often termed "radar facies" (Neal, 2004). We observe three radar facies. The first facies, observed where interfluves cross the road, exhibited reflections that are planar or wavy and are either spatially continuous or semi-continuous such as those shown in Figure 5a and 5b, Figure 6c, Figure 8a, 8b or 8e). The second facies, observed where valleys cross the road, is characterized by areas of chaotic and discontinuous reflectors such as those shown in portions of Figures 4c. Finally, we also observed a third facies characterized by areas with an absence of differentiated reflection events such as those depicted in Figure 4a (i.e. coinciding with the location of well LGW1) or Figure 4c (i.e. in between valley areas). To interpret such radar facies required observations from drillholes, auger holes and outcrops. This is most apparent in Figure 4 where an outcrop

allowed one-to-one identification of GPR facies. GPR and drilling/outcrop observations show

a strong consistency in several ways: 1) vertical sequences of GPR reflectors match with

alternating sequences of lithological interfaces as depicted in well LGW2 (Figure 5b); 2)

GPR reflections are lacking in areas where no lithological interfaces were observed in

recovered drill material (i.e. well LGW1 in Figure 4c); and 3) inferred EM wave velocities

from GPR were consistent with the lithologies detected from wells and outcrops. This latter

consistency can be observed both in 1D such as the contrast between Figure 4b and Figure

5b, or in 2D such as demonstrated in Figure 6b. It is also important to consider that signal

attenuation due to material properties will also result in lack of reflections as explained

below.

Our results not only show the ability of GPR collected in several modes to replicate

what is detected at single direct point measurements (i.e. auger holes), but also shows that

single point measurements may be fairly representative of the lateral variability of the critical

zone structure in certain locations while not in others. For example, lithological

characterization as determined at wells LGW2A and LGW2B (Figure 5) shows a fairly

consistent lateral distribution of materials that are also reflected in the overall lateral

continuity of reflectors shown along the GPR profile in Figure 5 (i.e. over 70 m long). On the

other hand, Figure 4 shows the opposite, and depicts how laterally variable the subsurface can

be at certain locations (i.e. valley areas vs. the rest as depicted in Figure 4c), and how most

likely auger hole results may differ radically when drill locations change even if just a few

meters. In that regard, and although a detailed correlation of the coring and GPR record is

beyond the scope of this paper (particularly when considering: 1) how the width of the

Fresnel zone dictates resolution, as explained earlier in the GPR methodology section, and 2)

the differences in terms of resolution between the drillings and the GPR), the results shown in

Figure 6 exemplify the unique potential of the method for better defining spatial variability in

EM wave velocity as related to changes in lithology. It is important however to consider that the resolution provided in Figure 6b was not feasible for all surveys and was possible in that particular location for two main reasons: 1) the use of higher frequency antennas (i.e. 200 and 160 MHz); and 2) the unique presence of numerous diffraction hyperbolae in the GPR common offset that allowed for a direct velocity estimation.

The presence of a reflector represents a contrast in dielectric permittivity related to lithology, water content, fracturing or other physical attributes. We interpret the reflectors imaged at the Luquillo sites mainly as lithological interfaces (such as alternating sequences of corestones and more altered regolith as exemplified in Figure 5), or the presence of rindlets and fracturing (as exemplified in Figure 6). For example, the presence of thick rindlet zones in Figure 6 corresponds to areas with GPR reflections likely due to changes in lithology, material density, or water content. It is important to note, however, that as described by Buss et al. (2008), the uppermost portion of each rindlet set grade upward into saprolite and sometimes ghost rindlets are observed in the saprolite. For that reason, saprolite near the corestones may sometimes retain contrasts in dielectric permittivity due to rindlet formation or alteration. In that case, such fabric in the saprolite may also result in GPR reflections. Similarly, corestones may also contain incipient fractures or weak zones that could result in GPR reflections. That may be the case for example for the dense reflector record shown in Figure 5, particularly along the portions of quartz diorite detected in wells LGW2A and LGW2B and resulting in internal reflections. Likewise, in the reflection record shown in Figure 8 for the most surficial materials at CD2 and EP1, reflections are visible, for the first few meters, that attenuate below 4–5 m. In multiple augered holes at those locations, mostly saprolite was recovered, but some holes hit refusal at shallower depths and this was attributed to buried rock fragments. Indeed, many angular hornfels rock fragments (up to half

meter in cross-section) were observed at the land surface. Thus, the GPR is likely imaging such corestones.

The results of the GPR surveys also provide a better understanding of the nature of EM wave propagation. First, the contrast between valley areas and the area surrounding well LGW1 (Figure 4) confirms the lack of reflections in the unfractured bedrock below 5 m - observed during drilling. The presence of bedrock below 5 m in interfluves is further confirmed by the high EM velocities detected below 5 m in the CMP (i.e. reaching 0.14 m ns^{-1} in Figure 4b). Lack of reflections associated with unfractured quartz diorite is also confirmed in Figure 6c, where lack of reflectors inside the corestones (i.e. no contrasts in dielectric permittivity to generate reflections) contrasts with the reflections recorded at rindlet zones. Second, surveys at the LGW2 wells (Figure 5) confirm that altered regolith (despite not having high electrical conductivity) may result in attenuation of the EM waves. Specifically, reflections are still visible down to a depth of 14 m into the column of material in Figure 5b, showing that GPR signal penetrates to those depths. Loss of signal finally occurs at depths that are consistent with the presence of an 8 m thick section of highly altered, saprolite-like regolith in well LGW2B. Attenuation due to the presence of saprolite (i.e. rather than natural attenuation of the signal with depth) is further confirmed when comparing Figure 5a and 5b. GPR signal is attenuated at approximately the same depth in the two figures despite the fact that the measurements were made at a point on the hillside about 4–5 m higher in Figure 5a compared to 5b. The signal penetrates deeper in Figure 5a than 5b despite that fact that the antenna in Figure 5a is located higher topographically; therefore, the attenuation must be occurring due to changes in material in the subsurface rather than depth-dependent attenuation. The presence of changes in regolith at depth that are detected by GPR is also confirmed in Figure 8, which documents that the GPR signal penetrated only 4–5 m despite the use of lower frequency antennas, i.e. 50 MHz (Figure 8a). In general, a lower

frequency will penetrate deeper that a higher frequency. This discrepancy is attributed to a change in composition or water content of the regolith at 4 or 5 m.

Given these interpretations, we now use the radar facies to infer the deep structure as distributed across the landscape. The lack of reflectors in the interfluve areas between the zones of chaotic reflectors is interpreted as zones where relatively unfractured bedrock is present at shallow depth. The type location for this facies was drilled at well LGW1, where one corestone was present above one putatively incipient corestone and ~20 m of unfractured rock.

The chaotic sequences of reflectors and presence of diffraction hyperbolas where the valley areas cross the road (Figure 4c) show sharp vertical boundaries that separate thick sequences of reflections up to 15–20 m deep versus areas of much shallower signal attenuation. Given that this GPR facies co-aligned with valleys crossing the road, we used aerial photographs to complete fracture trace analysis following standard methods (Lattman, 1958). Photography reveals that these valleys are aligned along the types of lineations usually interpreted as fractures. The GPR facies coincide where the lineaments cross Route 191. Based upon the GPR data, we infer that these features extend to significant depth beneath the surface, and are likely to contain weathered material including spheroidally weathering corestones at depths exceeding 20 m.

Route 191, where we completed the GPR measurements, is perched on a steep hillslope. The deep reflector zones were located where gullies or zero-order stream channels, i.e., headwater streams, cut sub-perpendicular to the road. To explore the nature of the cross-cutting fracture zones, we hiked down the cross-cutting gullies from the road. Often, about 3–4 meters of road fill were observed below the road in locations coincident with the areas of chaotic reflectors. Road fill thicker than a few meters in these small valleys is possible, but the road fill is not thick enough to explain the presence of ~20 m thick sequences of

reflectors. In contrast, it was not unusual to observe accumulations of corestones that had weathered out and/or rolled down the slope for tens of meters in these gully areas. In addition, one case shown in Figure 4c (the third area of reflectors located between 0–300ns and at a distance of 150m along the profile) coincided with the location of a landslide previously discussed by Kurtz et al. (2011). Given all these observations, the deep areas characterized by chaotic reflectors along the transect are attributed to deep zones of i) weathered material in situ, or ii) colluvial material delivered by landslides from upslope. In other words, these valley areas could either represent zones of formation or deposition of landslide-derived corestones.

To distinguish these two interpretations, we now place LGW2 in the context of these facies. LGW1 has been interpreted as a good representation of weathering in an interfluve (between fracture zones). In contrast, the topography at the LGW2 wells is consistent with its location at the upper elevation end of one of these headwater channels. It is also located where one of the lineaments observed on aerial photographs crosses Route 191. Thus, the complex subsurface composition at LGW2 indicated in the GPR and the drilling observations is considered representative of a deep vertical fracture zone. As discussed in Section 5.1, it is highly likely that both in situ weathering and colluvial processes are occurring in the material drilled by the LGW2 borehole. The deep GPR facies is thus attributed to deep vertical fracture zones that define lineaments crossing Route 191 and that host both in situ weathered material and colluvial material.

GPR velocities inferred from CMP surveys and the occasional presence of diffraction hyperbolas in CO profiles provide further information for subsurface characterization of the critical zone in Luquillo. For example, GPR surveys consistently depict the highest velocity values when in the presence of bedrock. At LGW1, for example, EM wave velocities estimated for unweathered rock (i.e. below the regolith-bedrock interface) average 0.11 to

0.14 m ns^{-1}. This is also consistent with the velocity estimates below 4–5 m at site PB as inferred from the CMP (Figure 7). These values correspond well with EM wave velocities typical for granitic/dioritic bedrock (Neal, 2004; Baker et al., 2007). EM wave velocities for the regolith are also consistent at all the quartz diorite sites, ranging between 0.06—0.09 m ns^{-1}. The contrast between EM wave velocity between bedrock and regolith is best shown in Figure 5: 1D velocity models yield velocities when transitioning from quartz diorite (reaching 0.11 m ns^{-1}) to quartz diorite-derived regolith (averaging 0.07 m ns^{-1}). Similarly, the PB outcrop in Figure 6 also depicts differences between low velocities of the saprolite and rindlet areas (averaging 0.065 m ns^{-1}) vs. higher velocities for the corestones (averaging 0.075 m ns^{-1}) and the deep bedrock below 4 or 5 m. In contrast, the EM wave velocities for the hornfels range slightly lower (i.e. 0.05—0.08 m ns^{-1}). Such slight differences between regolith on quartz diorite and regolith on the more mafic hornfels is likely related to differences in the composition of the material (i.e. clay content), physical properties (i.e., porosity), or water content. For example, the slightly slower wave velocity in regolith on hornfels is expected since some chlorite and illite were identified in the hornfels but not the quartz diorite regolith (Orlando, 2014). It thus may have a higher cation exchange capacity or water content.

5.3. Oxygen, the water table, and density of fractures

To put these results in context, we summarize the differences observed in composition and thickness of drilled borehole profiles with respect to watershed position in Table 1 and Figure 9. Topographically higher in the watershed or further from the knickpoint we observed: 1) the percentage of competent rock recovered from the borehole is lower; 2) the number of fractures detected in intact rock recovered from the borehole is lower; and 3) the range in variation in water table elevation is higher. Furthermore, both borehole measurements and GPR results show that when regolith is present, its thickness generally

increases from lower to higher elevations and with increasing distance from the knickpoint. Finally, the highest density of fractures in each borehole is located near the bedrock-regolith interface. Figure 9 sums up these trends in a schematic. In the figure, the knickpoint occurs just below LGW1 along the river profile. As depicted in Figure 9 based on drilling, the bedrock-regolith interface as we have observed it more or less parallels the land surface, except that the regolith depth generally increases toward the upper elevations, as does the depth to the water table.

In fact, the water table is possibly linked to the driver for the spheroidal fracturing and weathering that produces corestones throughout the watershed. The process that putatively creates rounded corestones in the Icacos watershed is expansion of biotite driven by the oxidation of Fe (II) at depths where oxygen can diffuse into unaltered rock (Fletcher et al., 2006; Buss et al., 2008). According to this model applied to LGW1, the rindlet-defining fractures at ~5 mbls are likely forming rapidly today due to the frequent fluctuations in depth of the water table that is focused at those depths (see blue band in Figure 3). As the water table lowers in the shallow, unconfined aquifer, pores drain and fill with atmospheric gases. When the water table rises again, O_2-containing gas in the newly saturated pores dissolves into the pore water (Holocher et al., 2002). The exposure of ferrous iron in biotite to oxygen-charged water then putatively causes expansion and micro-cracking (Fletcher et al., 2006; Buss et al., 2008). In LGW1 this water table variation is concentrated into the smallest depth interval as compared to the other boreholes, providing one explanation for the high density of rindlet fractures in that low elevation borehole.

Another potential explanation for the higher fracture density in LGW1 and LGW2 as compared to EP1 is that more oxygen infiltrates to the subsurface at the two lower elevations because of the generally thinner total regolith (Figure 3). The thick overlying column of ferrous mineral-containing, quartz-poor and clay-rich regolith at the highest location (EP1)

likely draws down oxygen in the infiltrating waters. Thus, in comparison to LGW1, water at

depth in the Fe-rich hornfels regolith high in the watershed at EP1 is likely not as oxygen-rich

as it infiltrates downward, slowing the formation of fractures by oxidation.

Given the large contrast in permeability between the unaltered bedrock and the

regolith, it is reasonable that this interface in every borehole experiences cycles of water

saturation and unsaturation – explaining the location of oxidation-driven fracturing and the

high density of fractures at the base of each borehole. In fact, the repeated fluctuation of the

water table may be integral to the process driving fracture formation because fluctuations

entrain O_2 into the porewaters of the rock (Holocher et al., 2002). In EP1 where regolith is

very thick, it is unlikely that the water table reaches as low as the bottom of regolith as

frequently as this occurs in LGW1. Deep signs of oxidation at EP1 may therefore document

very low water tables from periods of time in the past. Regardless, of all the boreholes, this

water-table cracking mechanism is likely most focused over a narrow depth interval in

LGW1.

Another explanation is also possible as to why the most concentrated number of

rindlets always lies directly above the bedrock in each borehole (i.e. Figure 3) and why fewer

fractures are observed overall in the EP1 borehole. Brocard et al. (2015) have reported

erosion rates as fast as 69 to 180 m My[-1] below the knickzone and as slow as 53 to 84 m My[-1]

above. Therefore, near the knickzone in LGW1, the time duration for weathering is shorter

because the erosion rate is driving faster movement of rock material through the weathering

zone faster; therefore, the fractures and rindlets are the youngest at this location. Therefore,

little time has elapsed since fracture formation in LGW1 and the rindlets subtended by

fractures have not yet weathered away. In contrast, at EP1, where erosion is slower and the

time duration represented in the entire regolith column is much longer, the fractures and

rindlets are likely forming at a slower rate as well as experiencing a longer duration of time to

weather away. Thus, older, shallower rindlets lying higher in the EP1 and LGW2 boreholes may largely have weathered away, explaining the relative scarcity of rindlets and rindlet-forming fractures higher in the profiles.

As presented in Section 5.1, it is also possible that the hornfels regolith is weathering more quickly at EP1 now than it did before weathering had advanced into the underlying quartz diorite. This is because once the felsic rock is penetrated, it no longer acts as an aquitard but rather allows overlying regolith to drain more rapidly. In well-drained soils, O_2 is entrained to greater depths. Eventually, the hornfels regolith is eroded off the land surface and the weathering of the quartz diorite accelerates even more as infiltrating waters provide more oxygen. Therefore, where downward percolation of oxygenated waters is not impeded by low-permeability and Fe-rich hornfels regolith (LGW1 and LGW2 (Figure 8)), weathering proceeds much faster in the deep quartz diorite than where hornfels regolith remains (EP1).

These ideas lead to a different explanation of the mechanism for knickpoint formation along Rio Icacos than has been recently published (Brocard et al., 2015). Specifically, the location of the knickpoint could be explained by the differences in weathering and erosion rates of the hornfels and quartz diorite. In fact, the knickpoint is located precisely in the only location where Rio Icacos crosses mapped hornfels bedrock (Figure 1c). At this point, Rio Icacos flows largely in a quartz diorite bedrock channel. According to this model, the knickpoint is an indicator of how recently that location was covered by hornfels on top of the quartz diorite. At the time when the knickpoint was positioned downriver from where it stands today, the location of today's knickpoint was still covered by hornfels and regolith like today's EP1. At that time, the weathering-induced fracturing of the underlying felsic rock was initiating but was slow (as observed today at EP1). Erosion remained relatively slow until the hornfels was removed, at which time weathering and erosion of the quartz diorite accelerated rapidly. The result is the ~2.5 km-wide knickzone. Remnants of the pre-existing

hornfels are observed in the Rio Icacos channel today at least as high as 580 masl and

hornfels is also inferred to cap the adjacent high-elevation topography. This explanation thus

relies on one very common theory for knickpoints, namely that knickpoints are often located

at interfaces between different lithologies. However, we invoke the idea that once the

overlying hornfels is removed, denudation of the underlying quartz diorite is so fast that most

of the evidence of the lithological contrast that originally controlled its position is removed,

with only clues in the uppermost ridges and in one location of the channel.

This study shows the importance of combining direct and indirect methods. For

example, observations from drilling are misleading without the GPR. The combination of

geophysics and drilling show that the regolith-bedrock interface is not a horizontal, laterally

continuous interface in the Rio Icacos watershed. Instead, some deep zones of vertical

fractures have intensified weathering and formation of corestones, have lowered the

topography locally, and have focused colluvial transport of corestones and saprolitic material.

The deep vertical fracture zones we observed are, for the most part, sub-perpendicular to

Route 191 (and thus the Rio Icacos). These zones may be where weathering and erosion are

fastest in the watershed.

6. Conclusions

A combination of GPR measurements and observations from drillings, augering and

exposed outcrops has elucidated some of the spatial distribution of subsurface materials in the

Rio Icacos. While direct methods provide 1-D (i.e. point) measurements at specific locations,

GPR surveys allow broader understanding of some of the spatial complexities. On the other

hand, GPR surveys cannot be adequately interpreted without drilling- or roadcut-derived

observations. In other words, our results show that GPR is consistent with observations at

individual boreholes, but that boreholes are not always representative of the whole critical

zone structure. Importantly, neither GPR nor drilling alone can reveal the critical zone architecture. In the Rio Icacos watershed, the regolith-bedrock interface is a complex, laterally discontinuous zone characterized by vertical fractures that promote infiltration of oxygenated water deep into the quartz diorite pluton. This process is most important once the hornfels contact aureole weathers away. This infiltration drives spheroidal weathering and formation of sub-spherical corestones. Where vertical fractures are spaced far apart in quartz diorite, the regolith is relatively thin on the intervening bedrock high (e.g., LGW1 on an interfluve). However, zones that contain many sub-vertical, closely spaced fractures allow deep weathering and corestone formation. These zones define topographic lows and are seen on aerial photographs as defining lineaments. The result of all these processes at a watershed scale is the general observation that when it is present, regolith is thicker at higher elevations. Rindlets and weathering-induced fracturing are concentrated in those areas closer to the knickpoint where variations in water table depth are focused into a smaller depth interval, bringing oxygen-charged water into contact with oxidizable rock. Near the knickpoint, the rate of disaggregation into corestones and rindlets is thus faster both because the overlying cap of iron-rich and impermeable hornfels-derived regolith has been removed but also because the cycling of the water table is much more focused over a small depth interval.

7. Acknowledgements

University of Pennsylvania) for help with field data acquisition. Giles Brocard and Ray

Fletcher are thanked for discussions of geological interpretations. We also thank and dedicate

this work to Fred Scatena (1954–2013) whose support made this work possible.

8. References

Annan AP. 2009. Electromagnetic principles of Ground Penetrating Radar. In *Ground Penetrating Radar Theory and Applications*, Jol H (ed). Elsevier Science; 544.

Baker GS, Jordan TE, Pardy J. 2007. An introduction to ground penetrating radar GPR. In *Stratigraphic Analyses Using GPR*, Baker GS, Jol HM (eds). Geological Society of America; 1-18.

Bazilevskaya E, Lebedeva M, Pavich M, Rother G, Parkinson DY, Cole D, Brantley SL. 2013. Where fast weathering creates thin regolith and slow weathering creates thick regolith. Earth Surface Processes and Landforms **38**: 847-858. DOI: 10.1002/esp.3369

Brantley SL, Buss H, Lebedeva M, Fletcher RC, Ma L. 2011. Investigating the complex interface where bedrock transforms to regolith. Applied Geochemistry **26, Supplement**: S12-S15. DOI: http://dx.doi.org/10.1016/j.apgeochem.2011.03.017

Brantley SL, Holleran ME, Jin L, Bazilevskaya E. 2013. Probing deep weathering in the Shale Hills Critical Zone Observatory, Pennsylvania (USA): the hypothesis of nested chemical reaction fronts in the subsurface. Earth Surface Processes and Landforms **38**: 1280-1298. DOI: 10.1002/esp.3415

Braun JJ, Descloitres M, Riotte J, Fleury S, Barbiero L, Boeglin JL, Violette A, Lacarce E, Ruiz L, Sekhar M, Mohan Kumar MS, Subramanian S, Dupre B. 2009. Regolith mass balance inferred from combined mineralogical, geochemical and geophysical studies: Mule Hole granitic watershed, South India. Geochimica Cosmochimica Acta **73**:

Brocard G, Willenbring JK, Scatena FN, Johnson AH. 2015. Effects of a tectonically-triggered wave of incision on riverine exports and soil mineralogy in the Luquillo Mountains of Puerto Rico. Applied Geochemistry **In Press**:

Brown S, Lugo AE, Silander S, Liegel L. 1983. Research history and opportunities in the Luquillo Experimental Forest. In *USDA Forest Service General Technical Report SO-44, Southern Forest Experiment Station*: New Orleans, Louisiana.

Buss HL, Brantley SL, Scatena FN, Bazilievskaya EA, Blum A, Schulz M, Jiménez R, White AF, Rother G, Cole D. 2013. Probing the deep critical zone beneath the Luquillo Experimental Forest, Puerto Rico. Earth Surface Processes and Landforms **38**: 1170-1186. DOI: 10.1002/esp.3409

Buss HL, Sak PB, Webb SM, Brantley SL. 2008. Weathering of the Rio Blanco quartz diorite, Luquillo Mountains, Puerto Rico: Coupling oxidation, dissolution, and fracturing. Geochimica et Cosmochimica Acta **72**: 4488-4507. DOI: http://dx.doi.org/10.1016/j.gca.2008.06.020

Cassidy NJ. 2009. Electrical and magnetic properties of rocks, soils, and fluids. In *Ground Penetrating Radar: Theory and Applications*, Jol HM (ed). Elsevier: Amsterdam, The Netherlands; 41-72.

Chaudhuri A, Sekhar M, Descloitres M, Godderis Y, Ruiz L, Braun JJ. 2013. Constraining complex aquifer geometry with geophysics (2-D ERT and MRS measurements) for stochastic modelling of groundwater flow. Journal of Applied Geophysics **98**: 288-297. DOI: 10.1016/j.jappgeo.2013.09.005

Cox DP, Marvin RF, M'Gonigle JW, McIntyre DH, Rogers CL. 1977. Potassium-argon geochronology of some metamorphic, igneous and hydrothermal events in Puerto Rico and the Virgin Islands. Journal of research of the US Geological Survey **5**: 689-703

Daniels DJ. 2004. Ground Penetrating Radar, 2nd Edition. Institution of Engineering and Technology

Dasios A, McCann C, Astin TR, McCann DM, Fenning P. 1999. Seismic imaging of the shallow subsurface: shear-wave case histories. Geophysical Prospecting **47**: 565-591

Dosseto A, Buss HL, Suresh PO. 2012. Rapid regolith formation over volcanic bedrock and implications for landscape evolution. Earth and Planetary Science Letters **337–338**: 47-55. DOI: http://dx.doi.org/10.1016/j.epsl.2012.05.008

Drake H, Tullborg E, MacKenzie AB. 2009. Detecting the near-surface redox front in crystalline bedrock using fracture mineral distribution, geochemistry and U-series disequilibrium. Applied Geochemistry **24**: 1023-1039

Fletcher RC, Brantley SL. 2010. Reduction of bedrock blocks as corestones in the weathering profile: Observations and model. American Journal of Science **310**: 131-164. DOI: 10.2475/03.2010.01

Fletcher RC, Buss HL, Brantley SL. 2006. A spheroidal weathering model coupling porewater chemistry to soil thicknesses during steady-state denudation. Earth and Planetary Science Letters **244**: 444-457. DOI: http://dx.doi.org/10.1016/j.epsl.2006.01.055

Harris SA. 1968. Nickpoint (Knickpoint). In *Geomorphology Encyclopedia of Earth Science*. Springer Berlin Heidelberg; 773-774.

Holbrook WS, Riebe CS, Elwaseif M, Hayes JL, Basler-Reeder K, Harry DL, Malazian A, Dosseto A, Hartsough PC, Hopmans JW. 2014. Geophysical constraints on deep weathering and water storage potential in the Southern Sierra Critical Zone Observatory. Earth Surface Processes and Landforms **39**: 366-380. DOI: 10.1002/esp.3502

Hunter JA, Pullan SE, Burns RA, Gagne RM, Good RL. 1984. Shallow seismic reflection mapping of the overburden-bedrock interface with the engineering seismograph; some simple techniques. Geophysics **49**: 1381-1385. DOI: 10.1190/1.1441766

Kurtz AC, Lugolobi F, Salvucci G. 2011. Germanium-silicon as a flow path tracer: Application to the Rio Icacos watershed. Water Resources Research **47**: W06516. DOI: 10.1029/2010wr009853

Larsen M. 1995. Use of Seismic Refraction Techniques for Investigating Recent Landslides in a Tropical Rain Forest in Puerto Rico. In *Energy and Mineral Potential of the Central American-Caribbean Region*, Miller R, Escalante G, Reinemund J, Bergin M (eds). Springer Berlin Heidelberg; 411-414.

Lattman L. 1958. Techniques of mapping geologic fracture traces and lineaments on aerial photographs. Photogramm Eng **24**: 568-576

Nahon DB. 1991. Self-organization in chemical lateritic weathering. Geoderma **51**: 5-13. DOI: http://dx.doi.org/10.1016/0016-7061(91)90063-Y

Neal A. 2004. Ground-penetrating radar and its use in sedimentology: principles, problems and progress. Earth-Science Reviews **66**: 261-330

Ogle CJ. 1970. Pollen analysis of sel-ected sphagnum bog sites in Puerto Rico. In *A tropical rain forest: a study of irradiation and ecology at El Verde, Puerto Rico*, Odum HT, Pigeon RF (eds); B135-B145.

Ollier CD. 1984. Weathering. Longman: London

Ollier CD. 1988. Deep weathering, groundwater and climate. Geografiska Annaler., Series A, Phys. Geog. **70**: 285-290

Orlando J. 2014. The anatomy of weathering profiles on different lithologies in the tropical forest of northeastern Puerto Rico: from bedrock to clouds. In *College of Earth and Mineral Sciences*. The Pennsylvania State University; 174.

Ruxton V, Bryan P, Berry L. 1959. The basal rock surface on weathered granitic rocks. Proceedings of the Geologists' Association **70**: 285-290. DOI: http://dx.doi.org/10.1016/S0016-7878(59)80010-9

Scatena FN. 1989. An introduction to the physiography and history of the Bisley Experimental Watersheds in the Luquillo Mountains of Puerto Rico. In *Gen. Tech. Rep. SO-72: San Juan, PR: U.S. Department of Agriculture, Forest Service, Southern Forest Experiment Station*; 22.

Schellekens J, Scatena FN, Bruijnzeel LA, van Dijk AIJM, Groen MMA, van Hogezand RJP. 2004. Stormflow generation in a small rainforest catchment in the Luquillo Experimental Forest, Puerto Rico. Hydrological Processes **18**: 505-530. DOI: 10.1002/hyp.1335

Seiders VM. 1971. Geologic map of the El Yunque quadrangle, Puerto Rico. U.S. Geological Survey.

Shafique M, van der Meijde M, Rossiter DG. 2011. Geophysical and remote sensing-based approach to model regolith thickness in a data-sparse environment. Catena **87**: 11-19. DOI: 10.1016/j.catena.2011.04.004

ten Brink U. 2005. Vertical motions of the Puerto Rico Trench and Puerto Rico and their cause. Journal of Geophysical Research: Solid Earth **110**: B06404. DOI: 10.1029/2004jb003459

ten Brink U, Marshak S, Granja JL. 2009. Bivergent thrust wedges surrounding oceanic island arcs: insights from observations and sandbox models in the north-eastern Caribbean plate. Geol. Soc. Am. Bull. **121**: 1522-1536

Turner BF, Stallard RF, Brantley SL. 2003. Investigation of in situ weathering of quartz diorite bedrock in the Rio Icacos basin, Luquillo Experimental Forest, Puerto Rico. Chemical Geology **202**: 313-341. DOI: http://dx.doi.org/10.1016/j.chemgeo.2003.05.001

Walker JW, Hulse WH, Eckart DW. 1973. Observations of the electrical conductivity of the tropical soils of western Puerto Rico. Geological Society of America Bulletin **84**: 1743-1752

White AF, Blum AE. 1995. Effects of climate on chemical weathering in watersheds. Geochimica et Cosmochimica Acta **59**: 1729-1747

White AF, Blum AE, Schulz MS, Vivit DV, Stonestrom DA, Larsen M, Murphy SF, Eberl D. 1998. Chemical Weathering in a Tropical Watershed, Luquillo Mountains, Puerto Rico: I. Long-Term Versus Short-Term Weathering Fluxes. Geochimica et Cosmochimica Acta **62**: 209-226. DOI: http://dx.doi.org/10.1016/S0016-7037(97)00335-9

Zhang J, Lin HS, Doolittle J. 2014. Soil Layering and Preferential Flow Impacts on Seasonal Changes of GPR Signals in Two Contrasting Soils. Geoderma **213**:
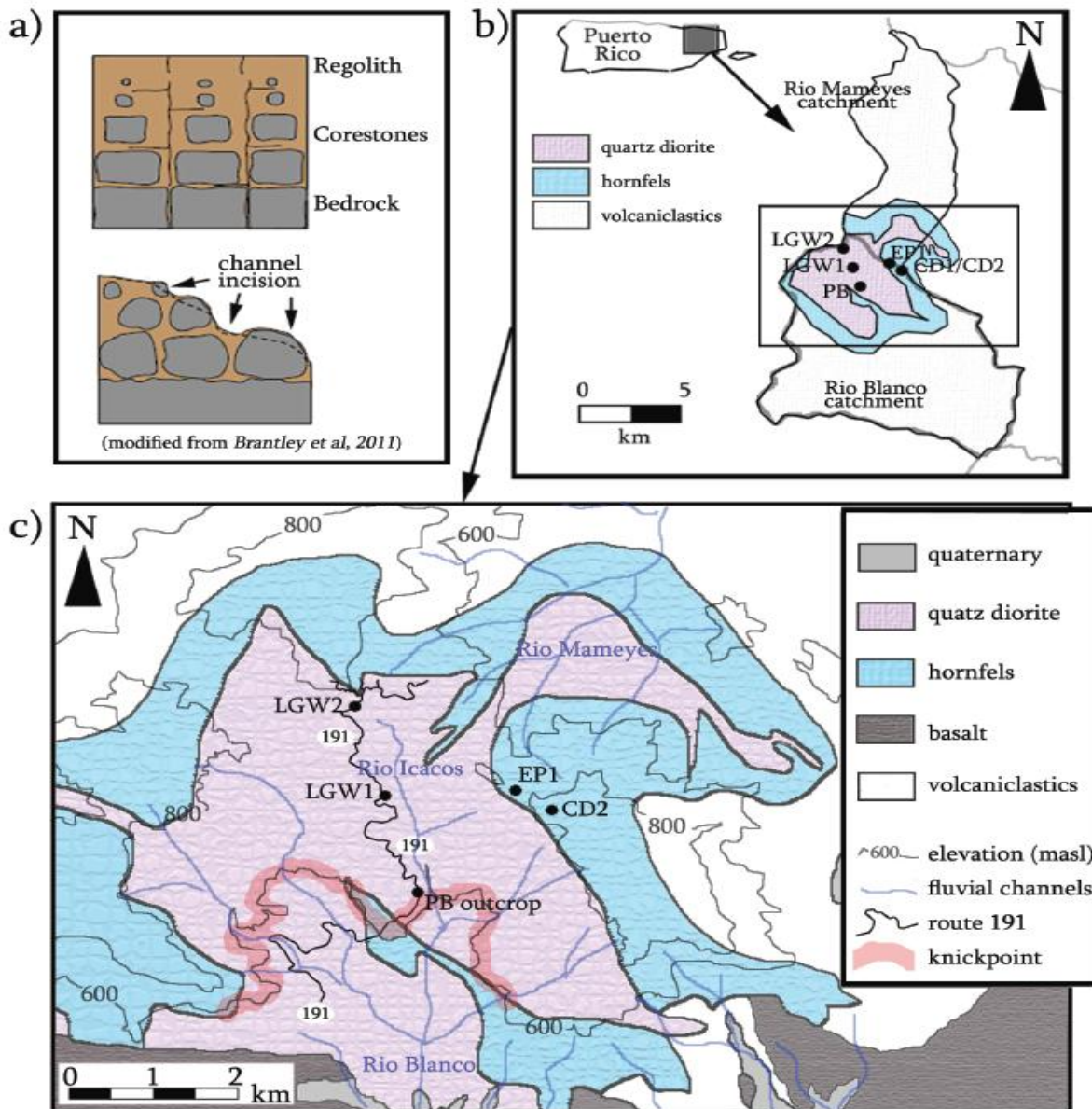
Figure Captions:

Figure 1

Figure 1: a) Conceptual model for spatial distribution of regolith, corestones and bedrock in the Luquillo Mountains before and after incision of a channel (modified from Brantley et al, 2011); b) map of Rio Blanco and Rio Mameyes catchment showing the location of fieldsites and distribution of geological materials within the study area; c) map of the Rio Icacos watershed showing location of study sites, topographic elevation, and geology. Approximate location of knickpoint as based on Brocard et al. (2015) is also shown.
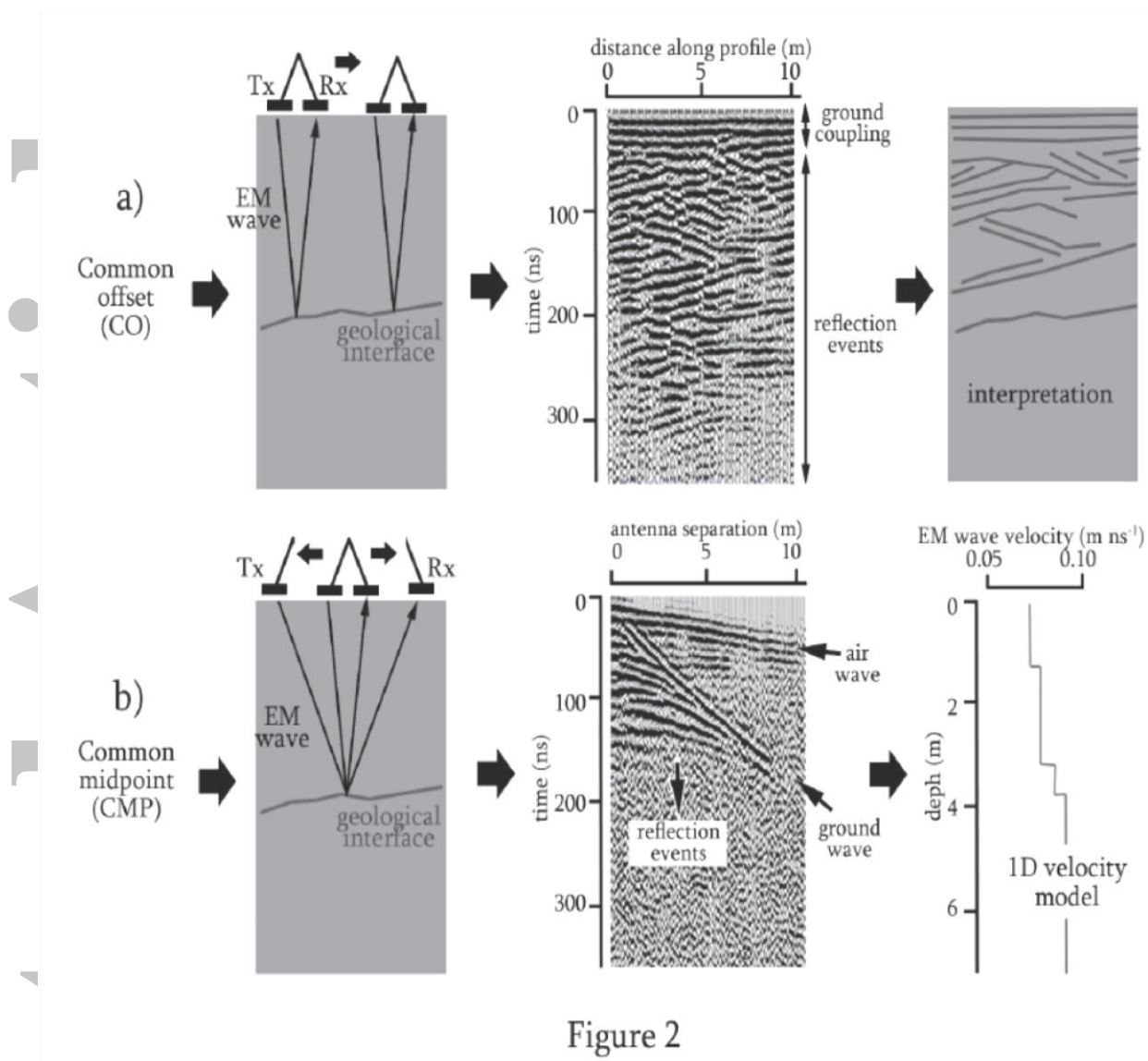
Figure 2: Diagram showing: a) the common offset (CO), and b) the common midpoint (CMP) GPR techniques. In each case a schematic of the geometry of the EM wave as it travels to a geological interface is shown together with a radargram that includes the main wavelet events (including ground coupling, air wave, ground wave, and reflection events). An idealized schematic of the interpreted cross-section from the CO and the 1D velocity model from the CMP is also shown.
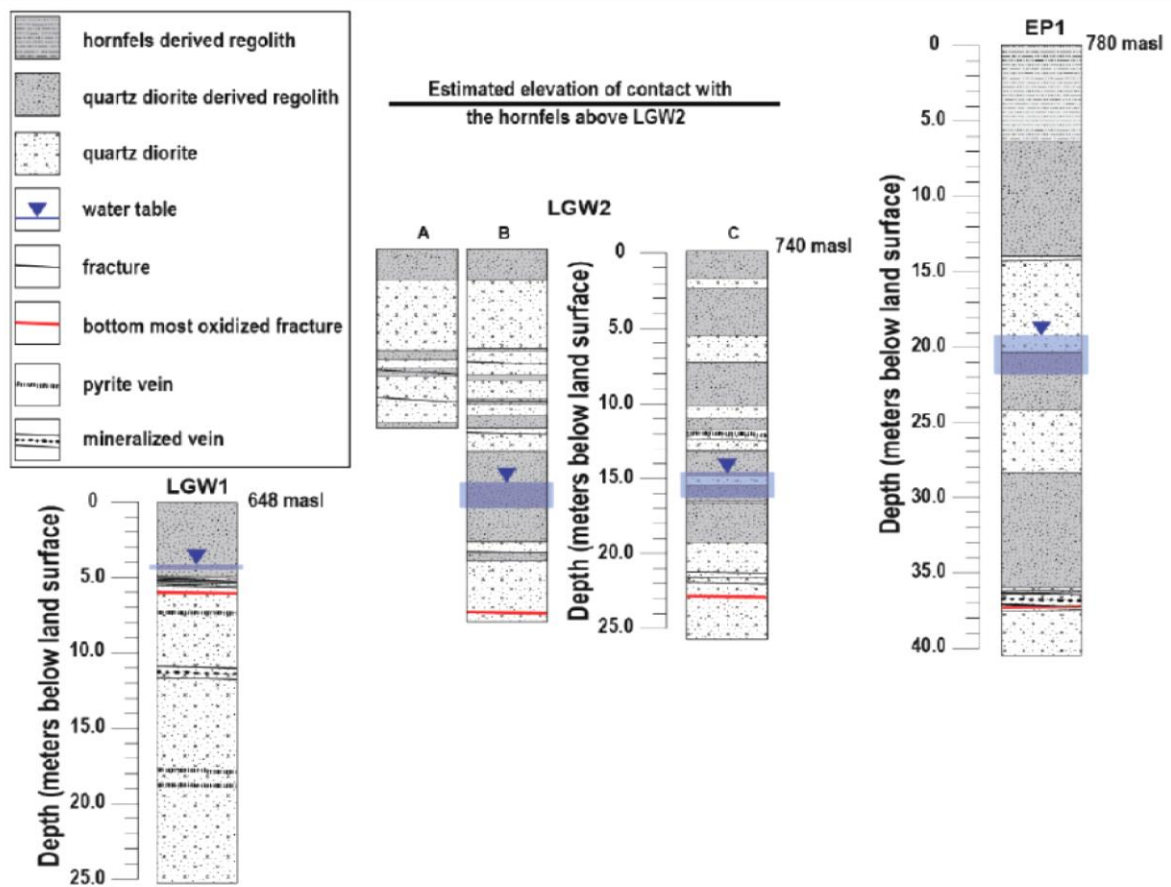
Figure 3

Figure 3: Summary of lithology and other elements inferred from drillings at each study sites. The values represent depth in meters below land surface. Elevation of each drilling location in meters above sea level (masl) is also shown. Observed variations in the water table are shown for each borehole in the shaded blue box below a downward facing triangle.
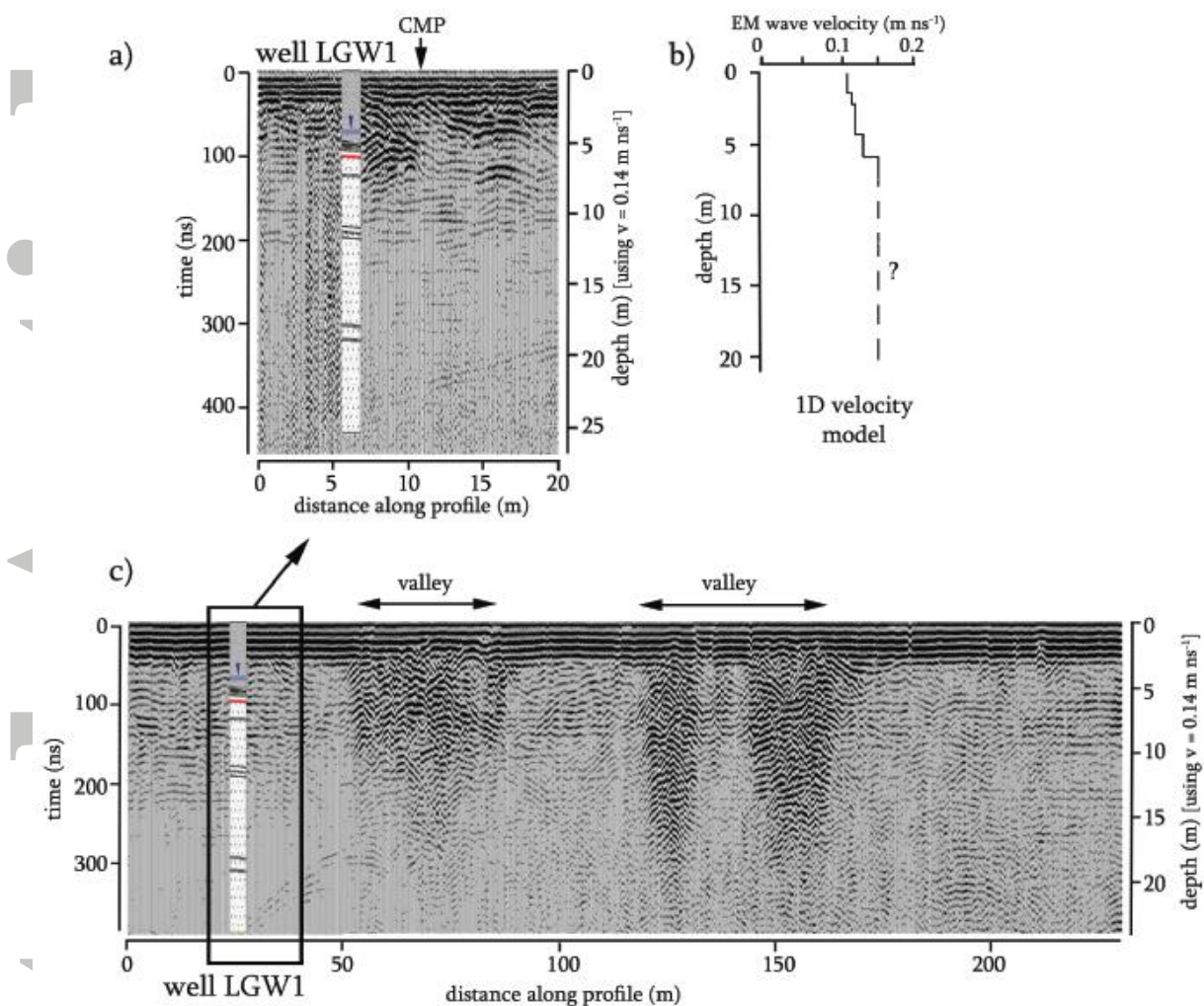
Figure 4

Figure 4: a) Common offset (CO) profile crossing well LGW1 (at about 6 m along profile) and b) inferred 1D velocity model from common midpoint (CMP) centered at 11 m along CO profile. An extended CO profile is shown in c) and shows the reflection record as it crosses several valley areas. Inferred lithologies and other elements for well LGW1 are also shown and follow the legend in Figure 3.
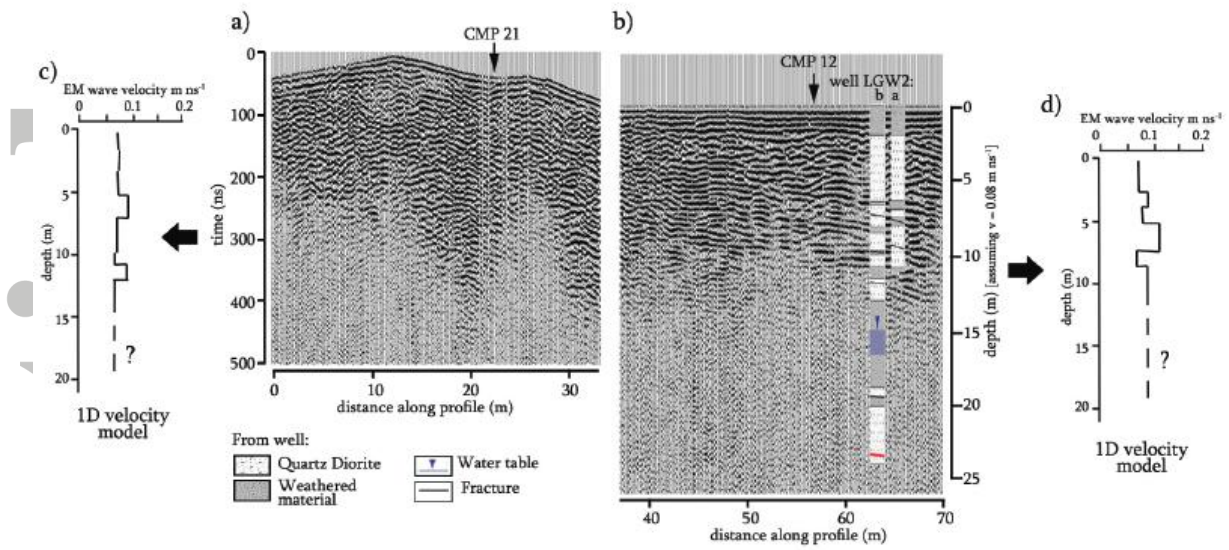
Figure 5

Figure 5: a) and b) Common offset (CO) profile crossing well LGW2A and LGW2B (at about 64 and 66 m along profile respectively); and c) and d) inferred 1D velocity model from common midpoint (CMP) profiles centered at 21 m and 58 m along CO profile. Inferred lithologies and other elements for wells are also shown.
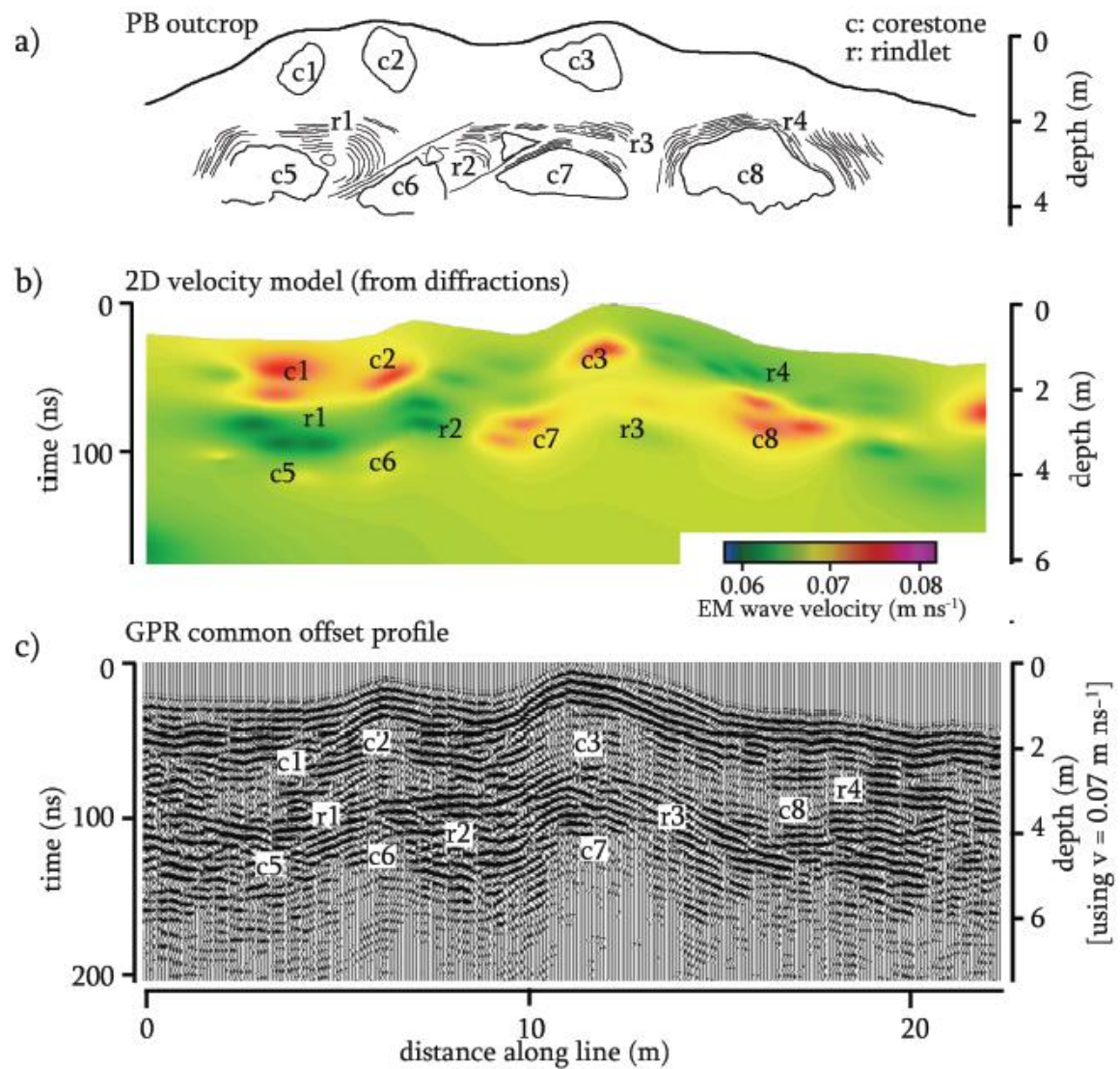
Figure 6

Figure 6: a) Schematic showing the spatial distribution of corestones (c1-c6) and rindlets (r1-r4) within the PB outcrop; b) 2D model of EM wave velocity (color scale indicates EM wave velocity) based on diffraction hyperbolas from a GPR common offset collected on top of the PB outcrop using a 160 MHz shielded antenna; c) GPR common offset profile collected on top of the PB outcrop using 200 MHz unshielded antennas. Location of corestones and rindlets in each case is also indicated.
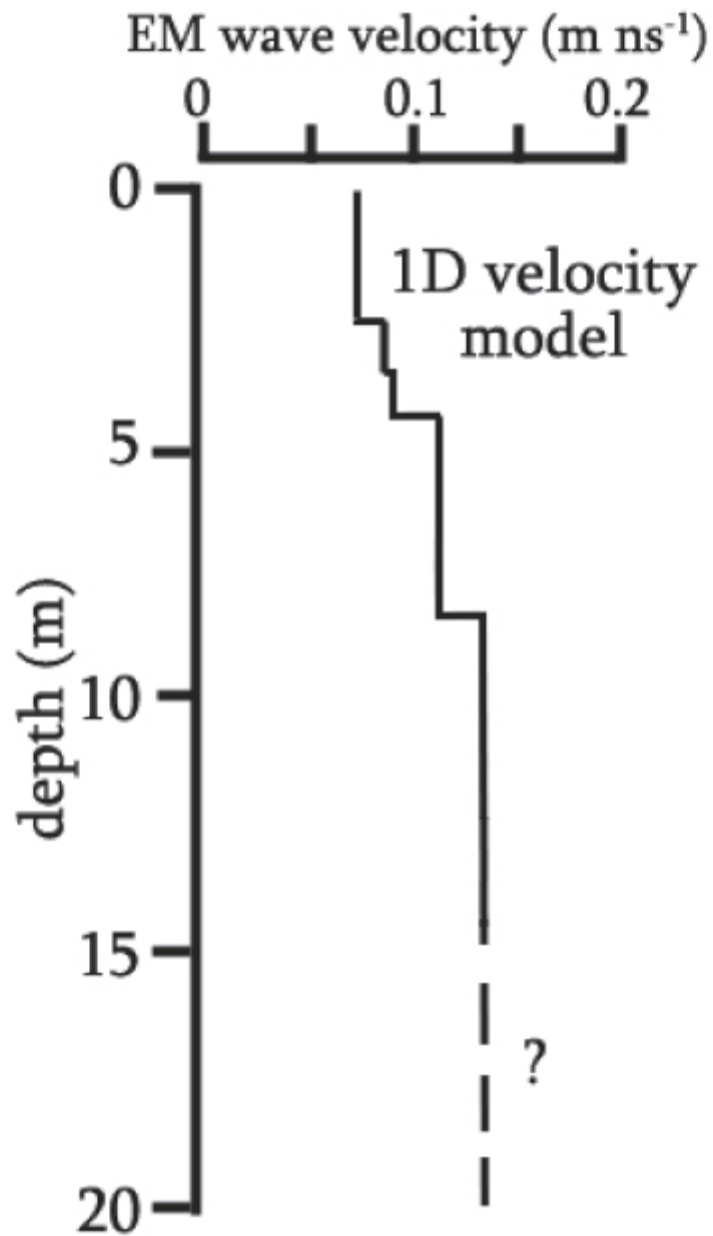
Figure 7

Figure 7: Inferred 1D velocity model for PB outcrop from common midpoint (CMP) profile centered at 6 m along CO profile in Figure 6c.
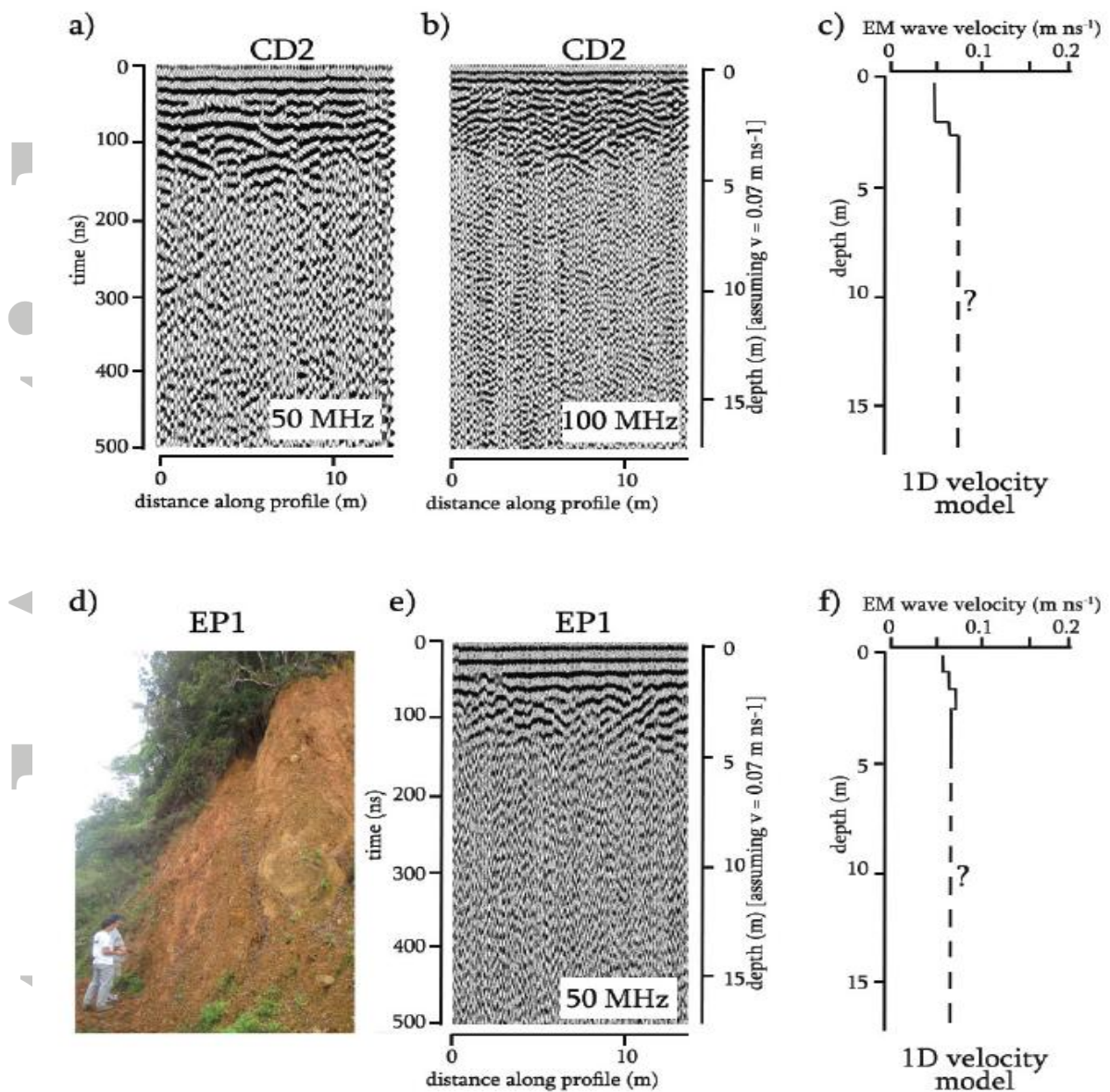
Figure 8

Figure 8: Common offset (CO) profile at site CD2 using a) 50 MHz unshielded antennas and b) 100 MHz unshielded antennas; c) inferred 1D velocity model from common midpoint (CMP) in the center CO profile; d) Photograph of 14 m outcrop exposure at site EP1 showing clay-rich regolith deposits; e) common offset (CO) profile at site EP1 using 50 MHz unshielded antennas; and f) inferred 1D velocity model from common midpoint (CMP) in the center CO profile at site EP1.
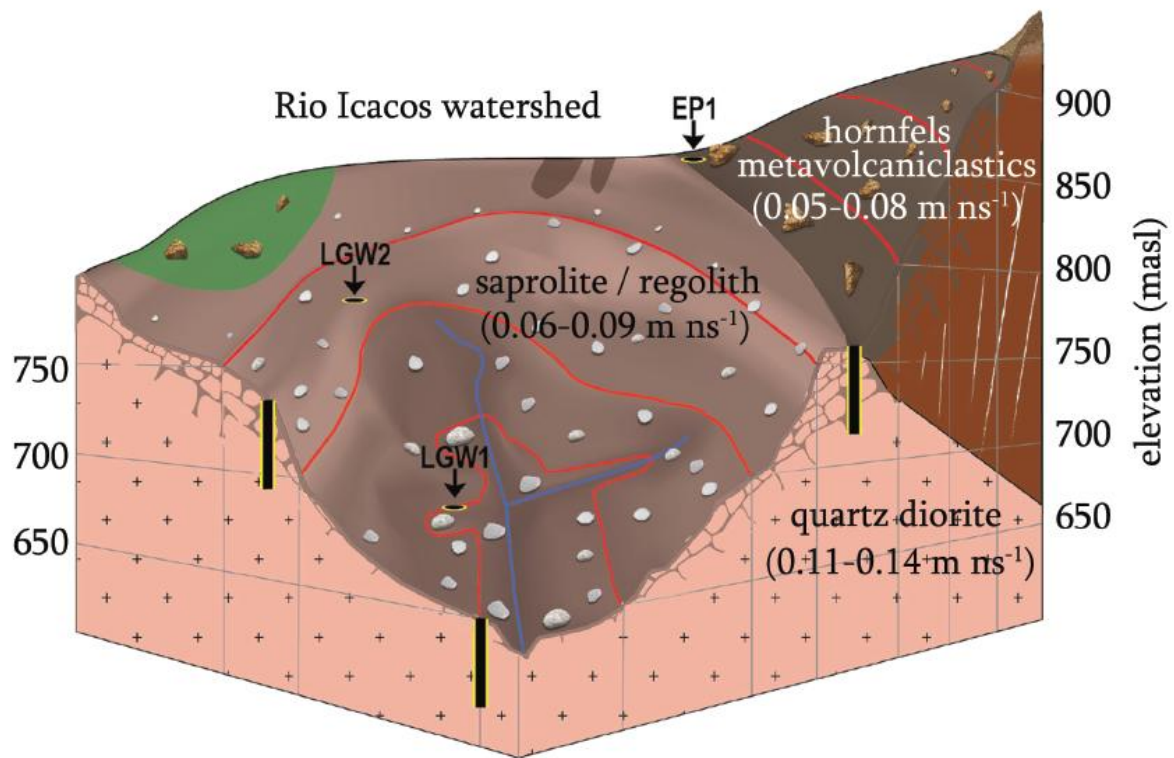
Figure 9

Figure 9: Conceptual model of the subsurface of the Rio Icacos watershed that includes drilling locations and range of EM wave velocity for each material.

Table 1: Summary of drilling sites, drilling observations, and recovered core.

Well	North	West	Total depth (m)	Distance to knickpoint (m)	Competent recovery (%)	Number of fractures / Fractures density (fracture/m)	Corestone size (avg) (observed in borehole, m)
LGW1	18.28225	65.78887	24.4	1,200	80	25 / 1.0	1
LGW2A			11.6		67	5 / 0.4	
LGW2B	18.29382	65.79167	25.3	2,900	57	12 / 0.5	2
LGW2C			26.0		42	16 / 0.6	
EP1	18.28258	65.77447	42.1	3,100	36	9 / 0.2	5